Comparison of four UAV georeferencing methods for environmental monitoring purposes focusing on the combined use with airborne and satellite remote sensing platforms

Joan-Cristian Padró[a,*], Francisco-Javier Muñoz[b], Jordi Planas[c], Xavier Pons[d]

[a] *Grumets Research Group, Departament de Geografia, Universitat Autònoma de Barcelona, Departament de Geografia Office B1092, Edifici B. Universitat Autònoma de Barcelona, 08193 Bellaterra, Catalonia, Spain*
[b] *HEMAV S.L. Edifici RDIT. Office 0007. C\Esteve Terrades, 1. Parc Mediterrani de la Tecnologia, 08860 Castelldefels, Catalonia, Spain*
[c] *Universitat Autònoma de Barcelona, Departament de Geografia Office B1092. Edifici B, Universitat Autònoma de Barcelona, 08193 Bellaterra, Catalonia, Spain*
[d] *Grumets Research Group, Departament de Geografia, Universitat Autònoma de Barcelona, Departament de Geografia Office B1094. Edifici B. Universitat Autònoma de Barcelona. 08193 Bellaterra, Catalonia, Spain*

ARTICLE INFO

ABSTRACT

This work is aimed at the environmental remote sensing community that uses UAV optical frame imagery in combination with airborne and satellite data. Taking into account the economic costs involved and the time investment, we evaluated the fit-for-purpose accuracy of four positioning methods of UAV-acquired imagery: 1) direct georeferencing using the onboard raw GNSS (GNSSNAV) data, 2) direct georeferencing using Post-Processed Kinematic single-frequency carrier-phase without in situ ground support (PPK1), 3) direct georeferencing using Post-Processed Kinematic double-frequency carrier-phase GNSS data with in situ ground support (PPK2), and 4) indirect georeferencing using Ground Control Points (GCP). We tested a multispectral sensor and an RGB sensor, onboard multicopter platforms. Orthophotomosaics at < 0.05 m spatial resolution were generated with photogrammetric software. The UAV image absolute accuracy was evaluated according to the ASPRS standards, wherein we used a set of GCPs as reference coordinates, which we surveyed with a differential GNSS static receiver. The raw onboard GNSSNAV solution yielded horizontal (radial) accuracies of RMSEr ≤ 1.062 m and vertical accuracies of RMSEz ≤ 4.209 m; PPK1 solution gave decimetric accuracies of RMSEr ≤ 0.256 m and RMSEz ≤ 0.238 m; PPK2 solution, gave centimetric accuracies of RMSEr ≤ 0.036 m and RMSEz ≤ 0.036 m. These results were further improved by using the GCP solution, which yielded accuracies of RMSEr ≤ 0.023 m and RMSEz ≤ 0.030 m. GNSSNAV solution is a fast and low-cost option that is useful for UAV imagery in combination with remote sensing products, such as Sentinel-2 satellite data. PPK1, which can register UAV imagery with remote sensing products up to 0.25 m pixel size, as WorldView-like satellite imagery, airborne lidar or orthoimagery, has a higher economic cost than the GNSSNAV solution. PPK2 is an acceptable option for registering remote sensing products of up to 0.05 m pixel size, as with other UAV images. Moreover, PPK2 can obtain accuracies that are approximate to the usual UAV pixel size (e.g. co-register in multitemporal studies), but it is more expensive than PPK1. Although indirect georeferencing can obtain the highest accuracy, it is nevertheless a time-consuming task, particularly if many GCPs have to be placed. The paper also provides the approximate cost of each solution.

1. Introduction

Capturing images by means of optical sensors installed in < 25 kg Unmanned Aerial Vehicles (UAV) or drones is gaining importance in quantitative remote sensing (Aasen et al., 2018), environmental research (Manfreda et al., 2018), remote sensing applications for vegetated areas (Komárek et al., 2018), precision agriculture (Borgogno Mondino and Gajetti, 2017), highly detailed metrology (Daakir et al., 2017) and cartographic (Crommelinck et al., 2017) applications. Moreover, their use in combination with other environmental remote sensing products, such as high Spatial Resolution (SR) satellite imagery (Lin et al., 2011) or airborne orthophotomaps of official mapping agencies (Whitehead and Hugenholtz, 2014) has attracted growing interest. In many European countries, current legislation allows a UAV to fly at a certain maximum height (e.g., 120 m in Spain (BOE, 2017). Consequently, commercial sensors usually provide SR between 0.01 m (1 cm) in RGB sensors and 0.10 m (10 cm) in multispectral sensors. A problem of this ultra-high SR is that it usually exceeds the accuracy of direct Exterior Orientation Parameters (EOPs) determination of individual images at the sensor exposure time, i.e., the positional (X,Y,Z) accuracy directly obtained from the platform onboard Global Navigation Satellite System (GNSS) receiver, and the sensor orientation (ω,φ,κ) directly obtained from the Inertial Measurement Unit (IMU) device. This particular process of determining EOPs for individual images at the exposure time entails an inaccurate georeferencing of the resulting orthophotomosaic, or at least an error largely exceeding the pixel size. The receiver rate of position measurements per second (Hz) is crucial for sampling the position of a mobile object; for example, at a velocity of 5 m/s, a 10 Hz GNSS receiver samples a position every 0.5 m. On the other hand, a receiver can work in code or carrier-phase mode, the latter usually provides more range accuracy, since the receiver is capable of distinguishing the sinusoidal wave oscillation where the signal code is located. This solution can be obtained in an expedient manner by using a single-frequency receiver. Moreover, the final accuracy can be improved by using a dual-frequency differential GNSS (DGNSS) receiver. A DGNSS is capable of reading two carrier-phases at two wavelengths (typically L1/L2) as well as consider signal delays caused by atmospheric effects (differential measurement). As reported by Colomina and Molina (2014), the Direct Georeferencing (DG) accuracy of a conventional UAV depends on the quality of the GNSS receiver; for example, in precision code, the positioning error can reach 0.77 m, and in the L1/L2 carrier-phase, the error can reach 0.01 m (Colomina and Molina, 2014). The code-based moderate accuracy is acceptable in UAV campaigns that only require low metric quality (Remondino et al., 2012). However, this imagery can neither be used to generate detailed cartography at large scales, such as 1:200 (ASPRS, 2014), nor be assumed to have reasonable pixel co-registration in multi-temporal studies using imagery with an SR < 0.1 m. A classic precise technique for accurate georeferencing of aerial imagery, known as Indirect Georeferencing (IG), consists of using Ground Control Points (GCPs) to support Aero-Triangulation (AT) and reaches accuracies of 0.02 m, which was evaluated by using Independent Check Points (ICPs) (Turner et al., 2014a, 2014b). IG was used in (Tian et al., 2017) to compare WorldView-2 imagery and UAV imagery. It provided pixel size accuracies of 1 cm RGB imagery and 7 cm multispectral (MicaSense RedEdge) imagery. Also (Zabala, 2017) used GCP to compare Sentinel-2 and MicaSense RedEdge data. The drawback is that taking data on the ground is not always feasible. When it is, it is very costly and entails a high volume of time and resources, which is ultimately not optimal or worth the overall investment of effort.

Post-Processing Kinematic (PPK) DG solution has been a widely used method in airborne platforms since 1990 (Skaloud et al., 1996). Recently, the market offers PPK solutions with devices light enough to be carried in < 25 kg UAV platforms. Consequently, PPK is an interesting option for remote sensing environmental users due to the accurate processing procedure after the flight (not in real-time, (Bisnath

et al., 2004). In environmental and topographic mapping projects, usually there is no requirement for Real-Time Kinematic (RTK) georeferencing. Nevertheless, it is important to obtain an imagery positioning that is as accurate as possible. This can be realized by post-processing the sensor central coordinates at the image exposure time, which takes into account the UAV trajectory, sensor position at trigger time (Rehak and Skaloud, 2017), satellite geometries and atmospheric error sources. The UAV trajectory is determined by interpolating the onboard GNSS data, whereby the sensor position at trigger time requires synchronizing between the camera and the onboard GNSS, and the GNSS satellite constellation information can be provided by Permanent Reference Stations (PRS) or Virtual Base Stations (VBS). This solution was tested in UAV platforms combining a single-frequency low cost GNSS receiver and IMU data (Turner et al., 2014a,b; Rehak et al., 2013), achieving accuracies almost similar to those of the typical spatial resolution of optical sensors suitable in a low-weight UAV for remote sensing applications. Other studies (Bláha et al., 2012; Rehak and Skaloud, 2015) analyzed the capacity of post-processing GNSS and IMU sensor integration data in UAV to outperform DG providing results of centimetric accuracies. Chio (Chio, 2016) evaluated a VBS RTK GPS-assisted self-calibration bundle adjustment for aerial triangulation of UAV images for updating 1:5000 topographic maps; he collected the data by flying a fixed-wing UAS mounted with a 24-mm focal-length Canon EOS 5D Mark II camera at 550 m, with 0.27 m in planimetry and 0.24 m in height accuracies (RMSE). In a later study, Chio and Lin (2017) tested a thermal camera mounted on a UAV using a Trimble BD970GNSS and PPK data that gave good preliminary results. All these aforementioned precedents use GNSS and IMU post-processed data to directly determine EOPs (X,Y,Z; ω,φ,κ) before the bundle adjustment phase. The determination of the image position still depends greatly on the GNSS receiver. Furthermore, the Integrated Sensor Orientation (ISO), which is commonly referred to as the pose of the image (Aasen et al., 2018; Wouda et al., 2016), is not a trivial procedure for a non-specialized user.

In our study, we compare the geometric accuracy of four different georeferencing techniques: (1) onboard Navigation GNSS (GNSSNAV); (2) PPK single frequency and the corrections of a permanent reference station located 4 km away from the flight area (PPK1); (3) PPK dual frequency and the corrections of a base station located in the flight area; and (4) Ground Control Points and Independent Check Points (GCP–ICP). The evaluation of GNSSNAV and PPK methods consisted of a comparison of image-derived coordinates with well-determined surveyed coordinates on specifically materialized targets used as ICP (RMSEx, RMSEy, RMSEr and RMSEz), while cross-validation was performed for the GCP–ICP method.

2. Materials and methods

2.1. Study area

We used the test area of the Can Gelabert farm (municipality of Riner, Catalonia) located northeast of the Iberian Peninsula, in the Mediterranean basin between the Catalan Central Depression and the Pre-Pyrenees. The planned study area has an area of 60 000 m^2 (6 ha), forming a rectangle having a side of 300 m in the E–W direction and a side of 200 m in the N–S direction. The altitude of the terrain at the materialized points is between 719.01 m and 734.20 m. The terrain morphology is not absolutely flat, as there are some unevenness formed by abandoned vineyards (including plain benches ranging from a minimum slope of 0° to a maximum slope of near 90° when moving from one bench to another) as well as trees higher than 8 m. In the central zone, there is a field of cereal crops, and the woody vegetation of the area is formed mainly by *Quercus humilis*, *Quercus ilex*, *Ulmus minor* and *Pinus nigra* ssp. *salzmanii*. The man-made elements consist of an 18th century rural complex, which includes the house of Can Gelabert (floor plan of 325 m^2), two haystacks, a pond and a small well.
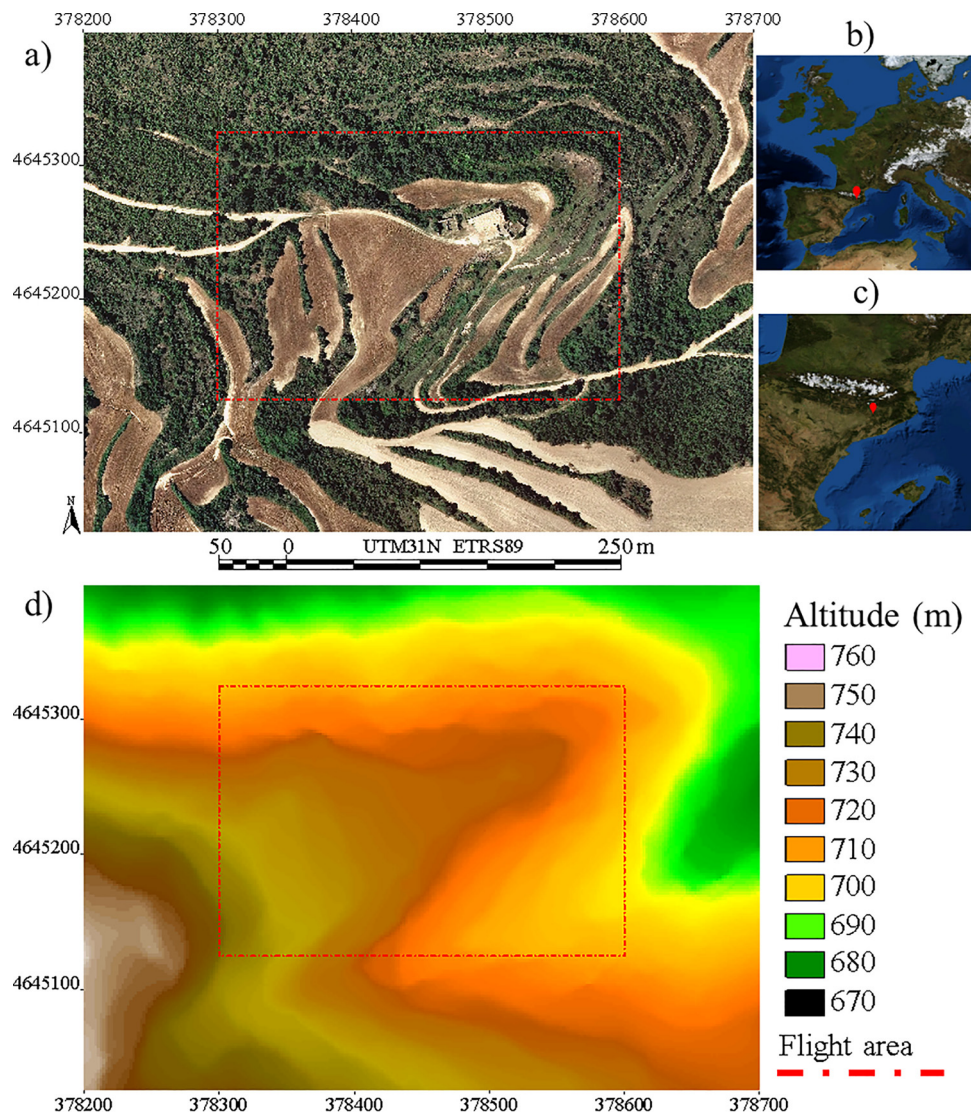
Fig. 1. a) Gelabert farm (Riner, Solsonès County). Red square shows the scope of the planned flight area. Background: Official cartography (SR = 0.25 m) (ICGC, 2018). b) Location of the area NE of the Iberian Peninsula. c) Location of the area in the European context. d) Digital Elevation Model of the planned flight area (Inverse Distance Weighted interpolation from official lidar cartography (SR = 2 m) (ICGC, 2018) (For interpretation of the references to colour in this figure legend, the reader is referred to the web version of this article).

A rural area, such as the one selected, proved to be an exemplary area for land cover mapping, environmental monitoring as well as for archeological purposes. Apart from this diversity, the test field followed the restrictions imposed by the Spanish aerial security agency (Agencia Estatal de Seguridad Aérea, AESA) (BOE, 2017), which prohibits flying UAVs in urban areas, in areas with large groups of people, or in the vicinity of aerodromes or airports (Fig. 1).

Eight flat concrete bases of 75 cm x 75 cm x 10 cm were purposely built within the study area in order to ensure the solidity and durability of these points. These bases, which were used as GCPs and ICPs, were distributed in the study area (Martínez-Carricondo et al., 2018) and covered the northing and easting ranges of the flight area. The location of the bases was planned to focus on the constructed complex and the main crop field surrounding the central flight area. The GCPs were all characterized by being located in plain areas not covered by vegetation. However, horizon visibility was not the same in all GCPs, as the sky view factor was > 89% in all GCPs, except in GCP Nr 7 (77%) (Table 1). These differences are important for the visibility of the satellites when measuring the GCP coordinates (Fig. 2).

A steel screw was placed at the center of each base to position the surveying rod used for determining the coordinate. A template was also created, wherein four quadrants of 25 cm could be easily painted on the base, thereby forming a checkered layout. This further ensured the necessary orthogonality for facilitating the location of the target center. A DGNSS static receiver, which was supported on a tripod with a clamp for high stability, was used to accurately determine the position of the GCPs (Fig. 3).

The DGNSS receiver (Leica Geosystems, 2017) can work with the information provided by a network of Permanent Reference Station (PRS), but this infrastructure has to be implemented in the region of the study area, as with the case of the European permanent reference station network (EUREF-EPN) (Ihde et al., 2014) or Continuously Operating Reference Stations (CORS) (Snay and Soler, 2008) in North America. For example, we used information from the PRS located in Solsona (SONA, http://catnet-ip.icc.cat/spiderweb/frmIndex.aspx), which is managed by the Institut Cartogràfic i Geològic de Catalunya (ICGC, 2017) and located about 4 km from our study area. The DGNSS measurements combined with the information of PRS allow the receiver's position to be determined more precisely than with RTK measurements. Nevertheless, these measurements require post-processing, and thus more time for obtaining the final positions. Continuous observation of the reference stations makes it possible to calculate

Table 1
Sky view factor (SVF) in the surveyed points used as reference coordinates.

Point-ID	Point-1	Point-2	Point-3	Point-4	Point-5	Point-6	Point-7	Point-8
SVF (%)	94.93	96.04	97.15	94.23	89.42	95.90	77.07	98.92

differential corrections to improve the accuracy of the broadcast orbits, the synchrony of the clocks of the satellites and receivers, and the modeling of ionospheric and tropospheric errors (Snay and Soler, 2008). PRS network data can be used in real time or in post-processing treatment.

2.2. Materials

The UAV platforms used were an octocopter (Fig. 4a) and a hexacopter (Fig. 4b). Both had a Pixhawk controller, which was assembled by the HEMAV Company to provide the team with more functionality and additional security measures (Table 2).

The octocopter was used to carry the SONY Alpha 7RII Digital Single-Lens Reflex (DSLR) camera (Table 3), which is sensitive in Red, Green and Blue (RGB) spectral regions, and included a 15-mm fixed lens (Voightländer, 2017). A memory card was located in the flash hotshoe, which recorded the GNSS time at the flash firing. The synchronization between the shooter rear curtain and flash firing is 1/250th of a second (Sony, 2017); the distance travelled by the UAV within this time at the programmed velocity (5 m/s) is 0.02 m.

The hexacopter was used to carry the multispectral and multilens MicaSense RedEdge camera (Table 4), which is sensitive to the RGB, red-edge and near-IR spectral regions (MicaSense, 2015). A port specifically intended for this purpose facilitated connection and synchronization between the camera and the GNSS device for recording the time in a memory card and geotagging the images.

The sensors were mounted on the gimbal of the corresponding platform. In the lab, the camera nodal point was aligned with the gimbal axis to prevent distortions in the lever-arm offsets when the gimbal compensates for the platform attitude angles. The lever-arm offset (X,Y,Z) between the Perspective Center (PC) camera position and the Antenna Phase Center (APC) was measured at a sub-centimetric level. The constant displacement vector (Skaloud et al., 1996) was further introduced in the post-processing software to compensate for the lever-arm offsets. Based on the corrected onboard GNSS signal and the time of image sensing, the PPK software interpolates the position of the camera PC camera position at the time of exposure, outputting the accurate estimation of every image PC position.

The photogrammetric software (Agisoft LLC, 2018) used in our

study has been widely used in previous studies to process UAV images and generate orthophotomosaics (Lucieer et al., 2014; Turner et al., 2014a,b; Zabala, 2017; Martínez-Carricondo et al., 2018). The photogrammetric software makes it possible to use automatically geotagged image PC to locate the individual images (DG) or set GCP to aerotriangulate the block (IG). In the case of geotagged image PC (post-processed or not) and IMU data (if provided), the photogrammetric software locates the frames in the map space, following the provided external position coordinates (X,Y,Z), and finds the optimal orientation angles (ω,φ,κ) between overlapped images by rotating, translating and scaling the individual frames. We followed the photogrammetric software workflow proposal developed by the United States Geological Survey (USGS) National Unmanned Aircraft Systems (UAS) Project Office (NUPO) for DSLR imagery (USGS-NUPO(a) (United States Geological Survey - National Unmanned Aircraft Systems Project Office), 2017) and MicaSense RedEdge multispectral imagery (USGS-NUPO(b) (United States Geological Survey - National Unmanned Aircraft Systems Project Office), 2017) for the purpose of obtaining 3D reconstruction from UAV photogrammetric imagery using Structure from Motion (SfM) techniques. A 3D point cloud was created, from which a Digital Surface Model (DSM) was generated. When the optimal correlation of homologous tie points was found to account for the perspective, an automatic camera calibration was achieved with the current environmental conditions, which used more points (> 1k) than in classic lab calibrations (Harwin et al., 2015). Then, the final georeferenced (UTM31 N ETRS89) orthophotomosaic at 0.025 m SR in Sony RGB imagery and at 0.05 m SR in MicaSense RedEdge multispectral imagery (Table 5) was exported to a remote sensing and GIS software (Microstation v 8i (Bentley Systems, 2017) and MiraMon v 8.01b (Pons, 2016)) so as to compare the image-derived coordinates to surveyed points. We used a different camera for one of the experiments in order to carry out a more thorough exploration in spectral and spatial resolutions. We are aware that using two cameras could introduce asymmetry in the experiment design. Nevertheless, we consider the varying results to substantially enrich the comparison part of the paper.

2.3. Methods

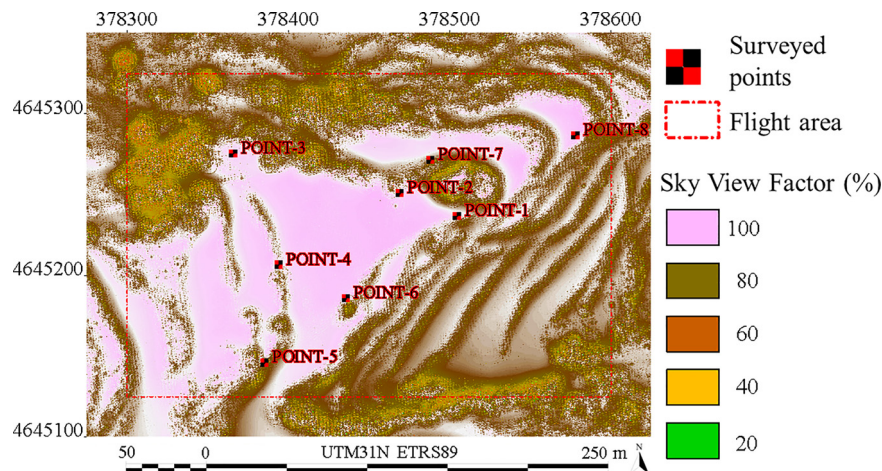The position of the GCPs was obtained by applying two

Fig. 2. Sky view factor map obtained from the Digital Surface Model (lidar official cartography (SR = 0.25 m) (ICGC, 2018) and the position of the Ground Control Points.
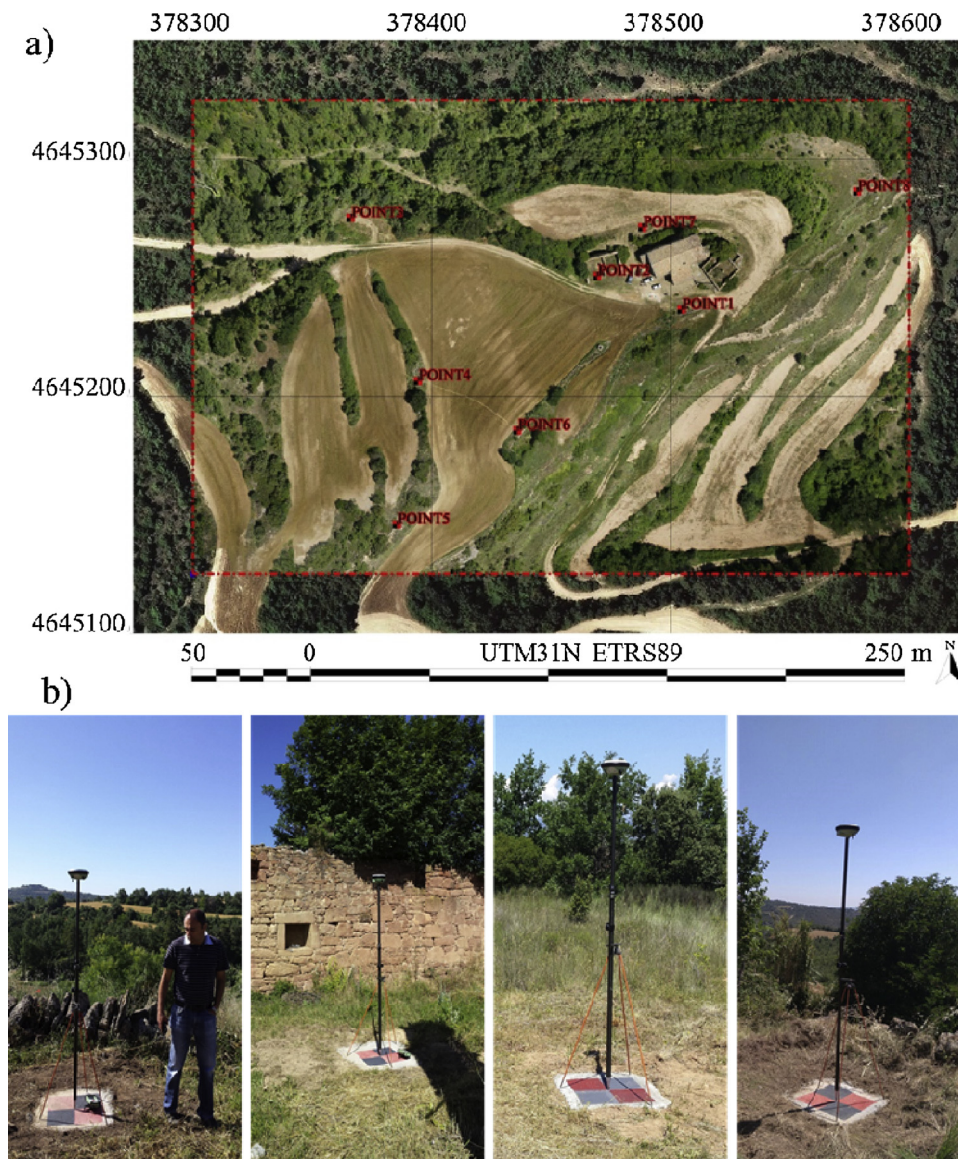
Fig. 3. a) The red rectangle indicates the distribution of surveyed GCPs on the orthophotomosaic generated with the PPK process (SR = 0.025 m). Background (outside the red rectangle): Official state-agency cartography (SR = 0.25 m) (ICGC, 2018). b) The DGNSS receiver, which was held on a tripod with a clamp, received measurements that were later analyzed in post-processing (For interpretation of the references to colour in this figure legend, the reader is referred to the web version of this article).

Fig. 4. a) Octocopter platform with the RGB sensor mounted on the gimbal; b) Hexacopter platform with the multispectral sensor mounted on the gimbal.

Table 2
UAV platforms and their main features.

Manufacturer-Model	Diameter Size (cm)	Flight autonomy (min)	MTOW (kg)	Optical sensor embedded type
DJI-S1000	105	15	11	RGB
DJI-S900	90	18	8.2	Multispectral

Table 3
SONY Alpha 7RII camera and its main features.

Manufacturer-Model	Size (mm)	Weight (g)	Raw radiometric resolution (bits) and expanded dynamic range (DN)	
SONY Alpha 7RII	127 × 96 × 60	625	12 (256 × 3 bands)	
Sensor type	Sensor size (pixels)	Pixel size (μm)	Focal Length (mm)	Bands
35 mm-CMOS	7952 × 5304	4.53	15	R-G-B

methodologies: firstly, all GCP measurements were made using static RTK, and secondly, the static DGNSS was set to collect data for a minimum of 20 min, which were post-processed (PP) to determine the most exact GCP position possible. Moreover, we opted to use RTK in order to expediently obtain coordinates that would be very similar to those calculated in the PP, thereby facilitating confirmation that the results obtained from the two methods are consistent because a priori PP measurements are much more reliable. In this study, we can see that the difference between the RTK and PP data is less than we expected, as it is horizontally almost always below 0.01 m, and vertically below 0.04 m (Table 6). However, for Point-7 there are larger variations between the two methods resulting in differences in X and Y of 0.06 m and 0.09 m, and 0.14 m in elevation.

Hence, the Point-7 position was considered not reliable enough to be taken as a reference. Thus, from the initial eight GCP we planned to use, we ultimately worked with the seven points that had well-known coordinates. Mean differences are 0.002 m in easting, 0.006 m in northing and −0.024 m in elevation (without considering Point-7).

The UAV georeferencing methods evaluation was carried out following the new ASPRS Positional Accuracy Standards for Digital Geospatial Data, which addresses recent innovations in digital imaging and non-imaging sensors, airborne GNSS, IMU and AT technologies (ASPRS, 2015). This standard defines accuracy classes based on RMSE thresholds for digital orthoimagery, digital planimetric data, and digital elevation data (ASPRS, 2015). Horizontal accuracy was assessed using $RMSE_X$ for the horizontal linear RMSE in the X direction (Easting), $RMSE_Y$ for the horizontal linear RMSE in the Y direction (Northing), and RMSEr for the horizontal linear RMSE in the radial direction, including both X- and Y-coordinate errors. Vertical accuracy was assessed using $RMSE_Z$ for the vertical linear RMSE in the Z direction (elevation). Note that vertical accuracy was evaluated as Non-Vegetated Area (NVA) RMSE statistics, since the GCPs were placed in vegetation-free locations. The threshold used to account for 95% of the error in the one-dimensional Z-axis over NVA was ≤1.96 x RMSE (ASPRS, 2015).

Horizontal and vertical thresholds (assuming normal distribution) established by ASPRS following the methodologies of the National Standard for Spatial Data Accuracy (NSSDA) FGDC, 1998) are shown in Table 7 (Table 7).

According to previous studies, in a simulation of populations, the high variability of NSSDA estimations is a result of the GCPs' sample size and population deviation (Ariza and Atkinson, 2008). In our case study, the relatively small sample size due to the limited extension of the study area led to a more conservative estimation, although the low population deviation seems to indicate otherwise. As our sample size is smaller than that of the Ariza and Atkinson (2008) simulations, we worked with NSSDA estimations. Indeed, for larger study areas and/or with more GCPs, those criteria proposed by Ariza and Atkinson could be applied.

The design basically consisted of checking the accuracy of the orthophotomosaics generated with the photogrammetric software using four different georeferencing methods, taking well-defined test points on the terrain as references, and comparing the results to the ASPRS standards. Finally, we proceeded to evaluate the differences between them, whereby we considered the estimated economic costs that can be amortized in several flight campaigns.

(1) GNSSNAV: The onboard navigation GNSS receiver used to determine the platform position works with the GPS/GLONASS constellations (using the European Geostationary Navigation Overlay System (EGNOS) augmentation system), L1/L2 frequencies with 20 channels, and a 10 Hz frequency rate (10 timestamps per second). The navigation GNSS method automatically geotags the central position (X,Y,Z) of the frames by recording the coordinates of the onboard GNSS APC at the closest trigger time (the offset between the APC and the PC was not accounted for), accordingly to the 10 Hz rate without differential correction. As previously introduced, at a velocity of 5 m/s, the positioning error due to this gap can range 0.5 m. In the photogrammetric software processing, we applied the workflow recommended by USGS for DSLR imagery (USGS-NUPO(a) (United States Geological Survey - National Unmanned Aircraft Systems Project Office), 2017). The derived orthophotomosaic absolute accuracy was validated with all the surveyed ICPs. The approximate economic cost of the GNSS device is less than 50 €. If direct positioning of images is applied, no time investment is necessary to process the onboard GNSS data. However, the photogrammetric software processing itself can take hours to determine the bundle block adjustment. Two PPK variants were used, which involved different hardware and fieldwork costs:

Table 4
MicaSense RedEdge sensor and its main features.

Manufacturer-Model	Size (mm)	Weight (g)	Raw radiometric resolution (bits) and expanded dynamic range (DN)	
MicaSense RedEdge	121 × 66 × 46	150	12 (0–65,535)	
Sensor type	Sensor size (pixels)	Pixel size (μm)	Focal Length (mm)	Number of bands
CCD	1280 × 960	3.75	5.5	5
#1 Blue FWHM (nm)	#2 Green FWHM (nm)	#3 Red FWHM (nm)	#4 Red-edge FWHM (nm)	#5 NIR FWHM (nm)
468–491	548–568	666–676	712–723	814–865

Table 5
Flight plan main features.

Platform and sensor	Side overlap (%)	Forward overlap (%)	Flight height (m)	Spatial resolution (m)	Georeferencing method
Octocopter -RGB	60	80	80	0.025	GNSSNAV; PPK2; GCP-ICP
Hexacopter Multispectral	60	80	80	0.050	PPK1

Table 6
Target coordinates (reference Ground Control Points) measured in the static Post-Processed (PP), and residuals with respect to Real-Time Kinematic (RTK) measurements.

TARGET COORDINATES UTM-31 N ETRS89 (m) POST-PROCESSED (PP)				RESIDUALS (m) PP *vs*. RTK		
Point-ID	X (Easting)	Y (Northing)	Z (Elevation)	Δ X (Easting)	Δ Y (Northing)	Δ Z (Elevation)
Point-1	378504.631	4645236.608	725.277	0.005	−0.001	−0.026
Point-2	378469.154	4645250.728	725.712	0.008	0.005	−0.012
Point-3	378366.020	4645275.324	726.314	0.008	0.006	−0.019
Point-4	378394.089	4645206.539	729.967	0.005	0.006	−0.014
Point-5	378385.341	4645145.964	734.201	−0.006	0.012	−0.037
Point-6	378435.762	4645185.649	728.625	−0.006	0.010	−0.036
Point-7	378488.194	4645271.260	723.034	−0.060	0.087	0.141
Point-8	378578.130	4645286.430	719.098	−0.004	0.005	−0.021

Table 7
Horizontal and Vertical (NVA) Accuracy Standards for Geospatial Data used to evaluate the four positioning methods.

Horizontal Accuracy at 95 % Confidence X, Y	Horizontal Accuracy at 95 % Confidence radial	Vertical Accuracy at 95 % Confidence Z (NVA)
≤ 2.4477 x $RMSE$	≤ 1.7308 x $RMSE_r$	≤ 1.9600 x $RMSE$

(2) PPK1: PPK1 method (Rokubun, 2018) consists of retrieving the PC camera position at the exposure time by calculating the flight path and interpolating the acquisition time of each image on the calculated trajectory. Argonaut 10 Hz single-frequency carrier-phase GNSS receiver with a 9-degree IMU embedded was used to obtain the position of the UAV. The triggering position was given by the onboard GNSS time sent to the camera MicroSD port, which was designed for this purpose. A Software as a Service (SaaS) (Rokubun, 2018) was used for data post-processing and determining the camera pose at exposure time, whereby we transferred the images and the MicroSD card data to the company by following online steps prescribed on their website (Rokubun, 2018). The PPK1 method, which requires the support of a PRS that continuously receives differential corrections and further corrects the onboard GNSS position, does not rely on any GCP or ground station in the study area. In the photogrammetric software processing, we applied the workflow recommended by USGS for multispectral imagery (USGS-NUPO(b) (United States Geological Survey - National Unmanned Aircraft Systems Project Office), 2017). The final orthophotomosaic absolute accuracy was validated with all surveyed GCPs. The approximate cost of the Argonaut receiver was 350 €, while the SaaS was 200 € (Rokubun, 2018).

(3) PPK2: PPK2 method (Drobit, 2017) proved to be the most sophisticated solution we tested and evaluated. The synchronization between the camera triggering and the GNSS time (Rehak and Skaloud, 2017) was carried out by a card device located in the flash support slit. Said card device collects the flash firing signal just before the rear curtain closes (flash is activated and synchronized with the rear curtain shutter). Drobit v1.6 software (Drobit, 2017), which was based on RTKlib open source libraries, was used for data processing in PPK2. During the post-processing stage, the lever-arm offsets were introduced in the software to obtain PC, instead of APC

coordinates. Although PPK2 can work with a PRS, as PPK1 does, we nevertheless used a station located at known coordinates in the study area to improve the local characterization of ionospheric, tropospheric and geometric errors affecting the L1/L2 carrier-phase GNSS signals. Thus, we were able to minimize the distance-dependent errors affecting the accuracy. The function of this base, which was linked to the nearest PRS, was to receive differential corrections continuously to further correct the onboard GNSS position. In the photogrammetric software processing, we applied the workflow recommended by USGS for DSLR imagery (USGS-NUPO (a) (United States Geological Survey - National Unmanned Aircraft Systems Project Office), 2017). The final orthophotomosaic absolute accuracy was validated with seven surveyed GCPs. Although this method does not rely on any GCP, it is nevertheless dependent on the base station located in the study area. The approximate cost of the rover module itself was about 4000 € and the base module was about 4500 € (Drobit, 2017).

(4) GCP–ICP: This method is not supported by onboard GNSS data. IG, which is a well-known technique based on AT, provides a bundle block adjusted to the ground references, and can therefore determine the EOP of each image block in an indirect way. The image orientation with photogrammetric software was done without using the imagery geotagged information. Rather, we manually located the GCP markers in their corresponding individual image. We performed cross-validation to validate the final orthophotomosaic's absolute accuracy, thereby generating seven orthophotomaps georeferenced with six GCPs; the remaining point was the ICP evaluated in each orthophotomap. Cross-validation (leave-one-out) consists of estimating a model from a subset, leaving an isolated value (test point) to perform the validation process, which is then carried out iteratively with all the data of the set (Picard and Cook, 1984). Assuming an accessible region of interest, the economic costs of materializing GCPs, including renting a static DGNSS and the personnel costs approximately amounted to 500 € The time invested was about one hour per GCP for painting and materializing concrete platform points; obviously, the time duration would be reduced if tarps were used or stable ground locations were painted. In our study, we took one hour for each GCP static GNSS measurement, two hours for post-processing static measurements and two processing hours for accurately locating GCPs in individual images.
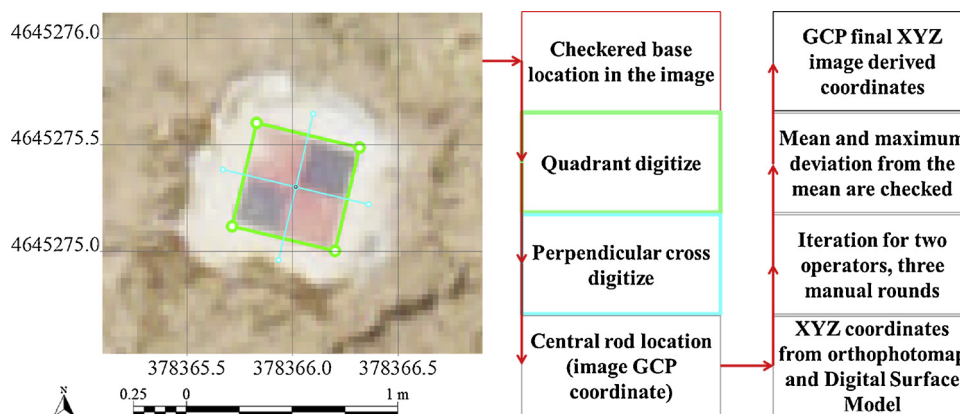
Fig. 5. Methodology for obtaining the image horizontal coordinates of GCPs (example for Point-3).

The coordinates in the resulting orthophotomosaics (image co-ordinates) were checked by two operators separately (Operator A and Operator B). In order to accurately determine the center of the target, i.e. the rod in the center of the concrete base, the procedure was based on digitizing the squared border (50 cm side) of the checkered area and drawing a centered cross. The coordinate of the crossing lines node was taken as the surveying rod coordinate in the image. Operator A per-formed this procedure twice, while operator B did a third round on the extraction of image coordinates. The mean value of the three manual rounds was the image value (see Table S1 Supplementary materials) compared with the reference surveyed coordinates. The image co-ordinates were considered valid if 90% of the coordinates have a dif-ference from the mean value less than one-third of the pixel size and the remaining 10% do not exceed half of the pixel size; otherwise, mea-surements had to be repeated. In the GCP-ICP cross-validation proce-dure, seven orthophotomaps were made, whereby one GCP was left out in each map, and Operators A and B extracted the coordinates of this point with the same described procedure (Fig. 5).

3. Results

The well-known surveyed coordinates of the GCP points (static DGNSS with post-processing) were compared with their estimated image-derived position for each method (Table 8). Calculation of one-dimensional (Easting, Northing or elevation) differences between the reference and the estimated values shows that the GNSSNAV method has the highest inaccuracies at all points, whereby PPK1 reduces the order of the error magnitude at all points, while GCP–ICP and PPK2 have very similar levels of accuracy at Point-3, but has clearly higher differences in the remaining points (Table 8). It is worth noting that the PPK2 results show a mean bias (similar to the pixel dimension of 0.025 m), but these values are not large enough to invalidate applying

the method in direct georeferencing of UAV imagery of very high re-solution. In fact, in other studies using NSSDA accuracy standards FGDC, 1998), we found clearly larger values when scale and pixel di-mension are compared.

The one-dimensional indicator of accuracy with respect to the re-ference points was positively checked for normality. As expected, the geometric errors in the univariate space (RMSE) were also of different orders of error magnitude between the different methods (Table 8). In the GNSSNAV option, the RMSE was under 1 m in X, 0.5 m in Y and over 4 m in Z, i.e. in the metric order; in the PPK1 option, the RMSE was up to 0.15 m in X, 0.20 m in Y and 0.24 m in Z, i.e. in the decimeter order; in the PPK2 option, the RMSE was up to 0.025 m in X or Y; and 0.036 m in Z; and in the GCP–ICP option the RMSE was up to 0.014 m in X, 0.018 m in Y and 0.030 m in Z, i.e. in the centimetric order (Table 9).

The synthetic indicator of planimetry precision, which assumed a normal distribution of the geometric errors in the XY bivariate space (combined in X and Y, or radial), showed a statistical error in 95% of the cases, i.e. 1.837 m in the GNSSNAV method, 0.443 m in the PPK1 method, 0.062 m in the PPK2 method, and 0.039 m in GCP-ICP method (Table 9). The radial indicator proved to be a robust method for determining the planimetric error, and thus for estimating the SR useful for each method, although the bivariate standard deviation of the errors was very valuable in obtaining the planimetric accuracy order of error magnitude of each method (Table 9).

4. Discussion

In this applied study, we used a lower number of GCPs than the number used in previous geometric accuracy evaluation studies (Ariza and Atkinson, 2008; Martínez-Carricondo et al., 2018). All the methods we tested have been proven to perform well in controlled situations. However, for this particular study, we used a realistic setting in UAV

Table 8
Residuals between reference coordinates (PP) and coordinates obtained using UAV positioning methods: (1) GNSSNAV, (2) PPK1, (3) PPK2, (4) GCP–ICP.

Positioning method	Point-ID	Point-1	Point-2	Point-3	Point-4	Point-5	Point-6	Point-8	μ	σ
1) Residuals (m) PP *vs.* GNSSNAV	Δ X	−0.946	−0.906	−0.845	−0.936	−1.001	−0.980	−0.938	−0.936	0.050
	Δ Y	0.436	0.476	0.604	0.528	0.511	0.511	0.398	0.495	0.067
	Δ Z	−4.257	−4.041	−3.591	−4.226	−4.652	−4.515	−4.095	−4.197	0.345
2) Residuals (m) PP *vs.* PPK1	Δ X	0.082	0.124	0.262	0.187	0.114	0.112	0.081	0.137	0.065
	Δ Y	−0.265	−0.272	−0.180	−0.116	−0.083	−0.219	−0.237	−0.196	0.074
	Δ Z	0.305	0.262	0.026	0.188	0.301	0.279	0.178	0.220	0.100
3) Residuals (m) PP *vs.* PPK2	Δ X	−0.030	−0.015	0.004	−0.016	−0.024	−0.034	−0.038	−0.022	0.014
	Δ Y	0.018	0.026	0.025	0.014	0.032	0.027	0.030	0.025	0.060
	Δ Z	−0.044	−0.010	−0.029	−0.032	0.028	−0.046	−0.045	−0.025	0.027
4) Residuals (m) PP *vs.* GCP-ICP cross-validation	Δ X	−0.012	0.008	0.013	0.007	0.007	−0.020	−0.023	−0.003	0.015
	Δ Y	−0.020	−0.002	−0.021	−0.008	−0.025	0.009	−0.025	−0.013	0.013
	Δ Z	0.017	0.023	−0.029	−0.030	0.022	−0.035	−0.046	−0.011	0.030

Table 9
RMSE in each of the univariate spatial components (X, Y and Z) and in the bivariate planimetric component (radial, combined XY) obtained using (1) GNSSNAV, (2) PPK1, (3) PPK2 and (4) GCP–ICP.

		RMSE	RMSE (95 % cases)
1) RMSE (m) GNSSNAV	X	0.937	1.837
	Y	0.499	0.977
	R (radial)	1.062	1.837
	Z	4.209	8.249
2) RMSE (m) PPK1	X	0.150	0.294
	Y	0.207	0.406
	R (radial)	0.256	0.443
	Z	0.238	0.467
3) RMSE (m) PPK2	X	0.025	0.050
	Y	0.025	0.050
	R (radial)	0.036	0.062
	Z	0.036	0.070
4) RMSE (m) GCP–ICP	X	0.014	0.028
	Y	0.018	0.035
	R (radial)	0.023	0.039
	Z	0.030	0.059

operational cases. Moreover, in our study, we learned that the field static measurements might result in proving the planned location of one GCP to be not reliable enough, such that this would have to be discarded, as in the case of Point-7.

Among the methods studied, the GCP-ICP method yielded the highest accuracy altogether. The PPK2 method, the PPK1 method and the GNSSNAV method yielded the second, the third and the fourth highest accuracies, respectively. Regarding the residuals (Table 8) and the image pixel size as a reference value, a clear bias is present in GNSSNAV and PPK1. These methods are not only less accurate in general terms, but they also provide a systematic displacement due to the combined error sources of the lever-arm offset, the lack of any ground reference point (GNSSNAV), or that this point was not close enough to our reference value (PPK1). Interestingly, the PPK2 and GCP–ICP methods, which had one or more ground reference points in the same study area, provided acceptable biases when compared with the reference value. Nevertheless, the economic cost, invested time and ground requirements of each method are different and can fit several remote sensing purposes. Note that even UAV imagery can be acquired at > 10 cm SR, and can thus be resampled to coarser pixel size to absorb geometric uncertainty, which is typically the radial error. Resampled imagery, which can be used to improve the processing of other remote sensing products, is not as detailed as drone-acquired imagery (Table 10).

The GNSSNAV method provided the poorer planimetric and altimetric accuracies, by overpassing 1 m. However, at an approximate cost of 50 €, GNSSNAV was the most affordable and the easiest-to-use option, and did not require ground or external support. Although this option is not useful for combining UAV imagery with satellite or airborne imagery < 2 m SR, it can nevertheless be useful for analyzing the intra-pixel features of airborne-acquired products of official mapping

agency at 2.5 m (ICGC, 2018; PNOA, 2018) or satellite sensors with coarser SR, such as the 10-m bands of MSI onboard Sentinel-2 (ESA, 2015), or the 15-m panchromatic bands of ETM + onboard Landsat-7 and OLI onboard Landsat-8 (NASA, 2018).

The PPK1 method, which improved the raw GNSS data by one order of error magnitude without in situ ground support, approximately costs 600 € (amortizable). Using PRS increases the accuracy due to the correction of the GNSS satellite signal. However, a post-processing service has to be additionally contracted. This option was accurate enough to combine UAV resampled imagery with the airborne-acquired products of official mapping agency at 0.25 m or 0.50 m SR, lidar data at 2 points/m^2(ICGC, 2018; PNOA, 2018), or sub-metric satellite imagery as the panchromatic band of WorldView-4 (Nadir: 0.31 m SR, 56° Off-Nadir: 1.00 m SR) (DigitalGlobe, 2018). However, it did not reach the goal of registering UAV imagery with SR > 0.05 m. Moreover, this method is not useful if PRS is not accessible within a radius of 20 km.

The PPK2 method, which approximately costs 8500 € (amortizable) was consistent enough in generating large-scale mapping from UAV imagery with less effort than the GCP–ICP method. The use of a station in the study area and a double-frequency receiver allows a better correction of satellite signal, and the synchronization of camera acquisition with the GNSS receiver is almost optimal. The cartographic quality that can be generated will depend on the specific norms applied. Nevertheless, it is clear that highly detailed maps (ASPRS, 2015; FGDC, 1998) can be produced with the PPK2 method. According to ASPRS tables (see Table 2), the goal of mapping at 1:200 scale with 5-cm SR imagery can be achieved in planimetry and in altimetry. Moreover, it seems that the UAV products processed with the PPK2 method constitute a valid alternative to the GCP–ICP method. However, such accuracy depends on the logistics of mounting a base station and in situ ground support.

Among all four methods studied, the GCP-ICP method proved to be the most accurate method. As far as the time invested and the economic costs involved, we spent one hour for static GNSS measurements for each GCP (displacing and setting the DGNSS) with specialized equipment (renting a DGNSS) and hiring a skilled personnel (500 €), and about two hours for post-processing the data. If GCPs materialized in concrete bases prove useful in future campaigns, as was the case in our study, then the process of materializing and painting the targets should be carried out the day before the flight. In our experience, the markers had to be placed in the corresponding images, which proved to be a tedious task that required over one hour. Apart from setting the GCPs, it is fair to note that the region of interest is not always accessible and this method is not useful in every case.

5. Conclusions

The positioning of UAV-acquired frame imagery can be solved by applying different methods with corresponding accuracies (ASPRS), economic costs and time investments. Aside from the multiple combinations of optical sensors, GNSS receivers, platforms, gimbals, and

Table 10
Summary of the pros and cons of the evaluated georeferencing methods.

	1) GNSSNAV	2) PPK1	3) PPK2	4) GCP–ICP
RMSE$_r$ (m)	1.062	0.256	0.036	0.023
RMSE$_z$ (m)	4.209	0.238	0.036	0.030
Approximate initial investment cost (€)	50	600	8500	500
Time consuming (h)	≥1	≥24	≥24	≥48
Involved personnel	≥1	≥1	≥2	≥2
In situ ground support	NO	NO	YES	YES
Suggested SR of the corrected imagery (m)	≥2	≥0.25	≥0.05	≥0.025
Examples of RS products to be combined with UAV data	Sentinel-2, imagery and coarser	WorldView imagery, airborne AHS, CASI, lidar data, and coarser	UAV Sequoia, Cubert data and coarser	UAV reflex cameras data and coarser
ASPRS associated maximum map scale	1:12000	1:1500	1:400	1:200

software that can be tested, we compared four commonly used georeferencing solutions in a real operational case for environmental remote sensing purposes with commonly used materials. Although the raw GNSS receiver direct georeferencing solution is not suitable for registering UAV data in different flight acquisitions, it is easy to use, can be purchased at a low cost, and does not require ground support, which is useful for visual inspections of remote sensing products with a pixel size coarser than 2 m, such as Landsat-like imagery. The Post-Processed Kinematic solution using single-frequency carrier-phase GNSS receiver and correcting GNSS signal with information from a permanent reference station located up to 20 km away, is valid for registering drone imagery with airborne lidar data or orthoimagery with a ground sampling distance of up to 25 cm. The Post-Processed Kinematic solution using double-frequency carrier-phase GNSS receiver and correcting the GNSS signal with information from a base station located in the study area, reaches the goal of registering UAV imagery at its common spatial resolution (≥ 5 cm). However, the logistics require the support of in situ materials and the cost is higher. The conventional indirect georeferencing using ground control points is the most accurate solution, as it is useful for registering UAV imagery with any other remote sensing coarser product. However, it also requires intense in situ ground support and is by far more time-consuming.

This study demonstrates that different UAV optical frame imagery georeferencing methods can be suitable and most effective when combined with conventional and freely available remote sensing products (e.g. Landsat, Sentinel-2, official mapping agencies lidar or orthoimagery). Obviously, the most accurate solutions are more expensive. Moreover, time and ground support are important factors to consider. Our paper is intended to be a quick and reliable guide for environmental scientists that provides a comparison of four known georeferencing methods to help them select the best option that suits their purpose, particularly in view of the accuracy required when combining UAV imagery with well-known airborne and satellite remote sensing platforms.

Author contributions

Conflicts of interest

Acknowledgments

Appendix A. Supplementary data

Supplementary material related to this article can be found, in the online version, at doi:https://doi.org/10.1016/j.jag.2018.10.018.

References

Aasen, H., Honkavaara, E., Lucieer, A., Zarco-Tejada, P.J., 2018. Quantitative remote sensing at ultra-high resolution with UAV spectroscopy: a review of sensor technology, measurement procedures, and data correction workflows. Remote Sens. 10, 1091–1933. https://doi.org/10.3390/rs10071091.

Agisoft LLC, 2018. PhotoScan User Manual, Professional Edition, Version 1.4.1. URL: (Last date accessed: 1 Oct. 2018). http://www.agisoft.com/pdf/photoscan-pro_1_4_en.pdf.

Ariza, F.J., Atkinson, A.D., 2008. Variability of NSSDA estimations. J. Surv. Eng. 134, 39–44. https://doi.org/10.1061/(ASCE)0733-9453(2008)134:2(39).

ASPRS (American Society for Photogrammetry and Remote Sensing), 2014. ASPRS Positional Accuracy Standards for Digital Geospatial Data. Edition 1, Version 1.0.0. URL: (Last date accessed: 1 Oct. 2018).. https://www.asprs.org/wp-content/uploads/2015/01/ASPRS_Positional_Accuracy_Standards_Edition1_Version100_November2014.pdf.

ASPRS (American Society for Photogrammetry and Remote Sensing), 2015. New Standards for New Era: Overview of the 2015 ASPRS Positional Accuracy Standards for Digital Geospatial Data. URL: (Last date accessed: 1 Oct. 2018). https://www.asprs.org/wp-content/uploads/2015/01/PERS_March2015_Highlight.pdf.

Bentley Systems, 2017. MicroStation, Version 8.1. URL: (Last date accessed: 1 Oct. 2018). https://www.bentley.com.

Bisnath, S., Wells, D., Santos, M., Cove, K., 2004. Initial results from a Long baseline, kinematic, differential GPS carrier phase experiment in a Marine environment. PLANS 2004 Position Location and Navigation Symposium. IEEE, Monterey, USA, pp. 625–631. https://doi.org/10.1109/PLANS.2004.1309052. 2004 Apr 26–29, Cat. No. 04CH37556.

Bláha, M., Eisenbeiss, H., Grimm, D., Limpach, P., 2012. Direct georeferencing of UAVs. ISPRS - International Archives of the Photogrammetry, Remote Sensing and Spatial Information Sciences, Volume XXXVIII-1/C22, 2011 ISPRS Zurich 2011 Workshop; 2011 Sep 14–16; Zurich, Switzerland. p. 131–136. https://doi.org/10.5194/isprsarchives-XXXVIII-1-C22-131-2011.

BOE (Boletín Oficial del Estado), 2017. "Real Decreto 1036/2017, de 15 de diciembre, por el que se regula la utilización civil de las aeronaves pilotadas por control remoto" [Royal Decree RD 1036/2017, of December 15, for the regulation of the civil use of remotely piloted aircrafts], vol. 316. Ministerio de Fomento, Madrid, Spain, pp. 129609–129641. BOE n URL: (Last date accessed: 1 Oct. 2018). http://www.boe.es/boe/dias/2017/12/29/pdfs/BOE-A-2017-15721.pdf.

Borgogno Mondino, E., Gajetti, M., 2017. Preliminary considerations about costs and potential market of remote sensing from UAV in the Italian viticulture context. Eur. J. Remote Sens. 50, 310–319. https://doi.org/10.1080/22797254.2017.1328269.

Chio, S.-H., 2016. VBS RTK GPS-assisted self-calibration bundle adjustment for aerial triangulation of fixed-wing UAS images for updating topographic maps. Bol Cienc Geod. 22, 665–684. https://doi.org/10.1590/S1982-21702016000400038.

Chio, S.-H., Lin, C.-H., 2017. Preliminary study of UAS equipped with thermal camera for volcanic geothermal monitoring in Taiwan. Sensors 17, 1649–1666. https://doi.org/10.3390/s17071649.

Colomina, I., Molina, P., 2014. Unmanned aerial systems for photogrammetry and remote sensing: a review. ISPRS – J. Photogramm. 92, 79–97. https://doi.org/10.1016/j.isprsjprs.2014.02.013.

Crommelinck, S., Bennett, R., Gerke, M., Ying Yang, M., Vosselman, G., 2017. Contour detection for UAV-Based cadastral mapping. Remote Sens. 9, 171–184. https://doi.org/10.3390/rs9020171.

Daakir, M., Pierrot-Deseilligny, M., Bosser, P., Pichard, F., Thom, C., Rabot, Y., Martin, O., 2017. Lightweight UAV with on-board photogrammetry and single-frequency GPS positioning for metrology applications. ISPRS – J. Photogramm. 127, 115–126. https://doi.org/10.1016/j.isprsjprs.2016.12.007.

DigitalGlobe, 2018. DigitalGlobe Products and Services. URL: (Last date accessed: 25 Jan. 2018). https://www.digitalglobe.com/#products.

Drobit, 2017. The Onboard Surveyor. A PPK Solution for Drone-mapping. URL: (Last date accessed: 1 Oct. 2018). https://www.drobit.es/drobit-specs-sheet.pdf.

ESA (European Space Agency), 2015. Sentinel-2A User Handbook. Released 24/07/2015. Rev.2 https://sentinels.copernicus.eu/web/sentinel/user-guides/document-library/-/asset_publisher/xlslt4309D5h/content/sentinel-2-user-handbook URL: (Last date accessed: 1 Oct. 2018).

FGDC (Federal Geographic Data Committee), 1998. Geospatial Positioning Accuracy Standards. Part 3: National Standard for Spatial Data Accuracy (NSSDA). URL: (Last date accessed: 1 Oct. 2018). https://www.fgdc.gov/standards/projects/accuracy/part3/chapter3.

Harwin, S., Lucieer, A., Osborn, J., 2015. The impact of the calibration method on the accuracy of point clouds derived using unmanned aerial vehicle multi-view stereopsis. Remote Sens. (Basel) 7, 11933–11953. https://doi.org/10.3390/rs70911933.

ICGC (Institut Cartogràfic i Geològic de Catalunya), 2017. Fonaments Del Posicionament Diferencial I Introducció a NTRIP" [Fundamentals of Differential Positioning and Introduction to NTRIP]. URL: (Last date accessed: 1 Oct. 2018). http://www.icgc.

cat/content/download/48729/337223/version/5/file/NTRIP_a_ICGC_%20v8.pdf.

ICGC (Institut Cartogràfic i Geològic de Catalunya), 2018. Aerial Photos and Orthophotos. URL: (Last date accessed: 1 Oct. 2018). http://www.icgc.cat/en/Public-Administration-and-Enterprises/Downloads/Aerial-photos-and-orthophotos.

Ihde, J., Habrich, H., Sacher, M., Söhne, W., Altamimi, Z., Brockmann, E., Bruyninx, C., Caporali, A., Dousa, J., Fernandes, R., Hornik, H., Kenyeres, A., Lidberg, M., Mäkinen, J., Poutanen, M., Stangl, G., Torres, J.A., Völksen, C., 2014. EUREF's contribution to national, European and global geodetic infrastructures. Proceedings of the IAG General Assembly 139, 189–196. https://doi.org/10.1007/978-3-642-37222-3_24. 2011 Jun 28–Jul 2.

Komárek, J., Klouček, T., Prošek, J., 2018. The potential of Unmanned Aerial Systems: A tool towards precision classification of hard-to-distinguish vegetation types? Int J Appl Earth Obs. 71, 9–19. https://doi.org/10.1016/j.jag.2018.05.003.

Geosystems, Leica, 2017. Leica Viva GS14 Technical Specifications. URL: (Last date accessed: 1 Oct. 2018). http://www.leica-geosystems.es/downloads123/zz/gpsgis/VivaGS14/brochures-datasheet/Leica_Viva_GS14_DS_en.pdf.

Lin, A.Y.M., Novo, A., Har-Noy, S., Ricklin, N.D., Stamatiou, K., 2011. Combining GeoEye-1 satellite remote sensing, UAV aerial imaging, and geophysical surveys in anomaly detection applied to archaeology. IEEE – J. Sel. Top. Appl. 4, 870–876. https://doi.org/10.1109/JSTARS.2011.2143696.

Lucieer, A., Turner, D., King, D.H., Robinson, S.A., 2014. Using an Unmanned Aerial Vehicle (UAV) to capture micro-topography of Antarctic moss beds. Int J Appl Earth Obs. 27, 53–62. https://doi.org/10.1016/j.jag.2013.05.011.

Manfreda, S., McCabe, M., Miller, P., Lucas, R., Pajuelo Madrigal, V., Mallinis, G., Ben-Dor, E., Helman, D., Estes, L., Ciraolo, G., et al., 2018. On the use of unmanned aerial systems for environmental monitoring. Remote Sens. 10, 641–669. https://doi.org/10.3390/rs10040641.

Martínez-Carricondo, P., Agüera-Vega, F., Carvajal-Ramírez, F., Mesas-Carrascosa, F.J., García-Ferrer, A., Pérez-Porras, F.J., 2018. Assessment of UAV-photogrammetric mapping accuracy based on variation of ground control points. Int. J. Appl. Earth Obs. 72, 1–10. https://doi.org/10.1016/j.jag.2018.05.015.

MicaSense, 2015. MicaSense RedEdge™ 3 Multispectral Camera User Manual. MicaSense, Inc., Seattle, WA, pp. 33. URL: (Last date accessed: 1 Oct. 2018). https://support.micasense.com/hc/en-us/article_attachments/204648307/RedEdge_User_Manual_06.pdf.

NASA (National Aeronautics and Space Administration), 2018. Landsat Data Continuity Mission (LCDM). URL: (Last date accessed: 1 Oct. 2018). https://www.nasa.gov/mission_pages/landsat/main/index.html.

Picard, R., Cook, D., 1984. Cross-validation of regression models. J. Am. Stat. Assoc. 79, 575–583. https://doi.org/10.1080/01621459.1984.10478083.

PNOA (Plan Nacional de Ortofotografía Aérea), 2018. Productos generados" [Generated products]. URL: (Last date accessed: 1 Oct. 2018). http://pnoa.ign.es/productos.

Pons, X., 2016. "MiraMon. Sistema d'Informació Geogràfica i software de Teledetecció. Versió 8.01b" [MiraMon. Geographical Information System and Remote Sensing software. Version 8.01b]. Centre de Recerca Ecològica i Aplicacions Forestals, CREAF. Bellaterra. ISBN: 84-931323-4-9. URL: http://www.creaf.uab.cat/miramon (Last date accessed: 1 Oct. 2018).

Rehak, M., Skaloud, J., 2017. Time synchronization of consumer cameras on Micro aerial Vehicles. ISPRS – J. Photogramm. 123, 114–123. https://doi.org/10.1016/j.isprsjprs.2016.11.009.

Rehak, M., Mabillard, R., Skaloud, J., 2013. A Micro-UAV with the capability of direct georeferencing. ISPRS - International Archives of the Photogrammetry, Remote Sensing and Spatial Information Sciences, Volume XL-1/W2, 2013 UAV-g2013; 2013 Sep. 4–6; Rostock, Germany 317–323. https://doi.org/10.5194/isprsarchives-XL-1-W2-317-2013.

Rehak, M., Skaloud, J., 2015. Fixed-wing micro aerial vehicle for accurate corridor mapping. ISPRS - Annals of the Photogrammetry, Remote Sensing and Spatial Information Sciences, Volume II-1/W1, 2015 International Conference on Unmanned Aerial Vehicles in Geomatics; 2015 Aug 30–Sep 02 23–30. https://doi.org/10.5194/isprsannals-II-1-W1-23-2015.

Remondino, F., Barazzetti, L., Nex, F., Scaioni, M., Sarazzi, D., 2012. UAV Photogrammetry for Mapping and 3d Modeling -current Status and Future Perspectives-. ISPRS - International Archives of the Photogrammetry, Remote Sensing and Spatial Information Sciences, Volume XXXVIII-1/C22, 2011 ISPRS Zurich 2011 Workshop; 2011 Sep 14–16, Zurich, Switzerland, pp. 1–7. https://doi.org/10.5194/isprsarchives-XXXVIII-1-C22-25-2011.

Rokubun, 2018. Argonaut Datasheet. URL: (Last date accessed: 1 Oct. 2018). http://rokubun.cat/wp-content/uploads/2017/12/ARGONAUT_Brochure.pdf.

Skaloud, J., Cramer, M., Schwarz, K.P., 1996. Exterior orientation by direct measurement of camera position and attitude. ISPRS - International Archives of Photogrammetry and Remote Sensing Vol. XXXI, Part B3; 1996 Jul 9–19; Vienna, Austria. P. 125–130. URL: (Last date accessed: 1 Oct. 2018). http://www.ifp.uni-stuttgart.de/publications/1996/wien96_gpsins.pdf.

Snay, R.A., Soler, T., 2008. Continuously operating reference stations (CORS): history, applications, and future enhancements. J Surv Eng. 134, 95–104. https://doi.org/10.1061/(ASCE)0733-9453(2008)134:4(95).

Sony, 2017. α7R e-mount Camera With Full Frame Sensor. Full Specifications and Features. URL: (Last date accessed: 1 Oct. 2018). https://www.sony.com/electronics/interchangeable-lens-cameras/ilce-7r/specifications#specifications.

Tian, J., Wang, L., Li, X., Gong, H., Shi, C., Zhong, R., Liu, X., 2017. Comparison of UAV and WorldView-2 imagery for mapping leaf area index of mangrove forest. Int. J. Appl. Earth Obs. 61, 22–31. https://doi.org/10.1016/j.jag.2017.05.002.

Turner, D., Lucieer, A., Malenovský, Z., King, D.H., Robinson, S.H., 2014a. Spatial Co-registration of ultra-high resolution visible, multispectral and thermal images acquired with a Micro-UAV over antarctic moss beds. Remote Sens. 6, 4003–4024. https://doi.org/10.3390/rs6054003.

Turner, D., Lucieer, A., Wallace, L., 2014b. Direct georeferencing of ultrahigh-resolution UAV imagery. IEEE Trans. Geosci. Remote 52, 2738–2745. https://doi.org/10.1109/TGRS.2013.2265295.

USGS-NUPO(a) (United States Geological Survey - National Unmanned Aircraft Systems Project Office), 2017. Unmanned Aircraft Systems Data Post-processing. Structure From Motion Photogrammetry. Section – 1 Digital Single-lens Reflex (DSLR) Imagery. URL: (Last date Accessed: 1 Oct. 2018). https://uas.usgs.gov/pdf/PhotoScanProcessingDSLRMar2017.pdf.

USGS-NUPO(b) (United States Geological Survey - National Unmanned Aircraft Systems Project Office), 2017. Unmanned Aircraft Systems Data Post-processing. Structure From Motion Photogrammetry. Section – 2 MicaSense 5-band Multispectral Imagery. URL: (Last date accessed: 1 Oct. 2018). https://uas.usgs.gov/pdf/PhotoScanProcessingMicaSenseMar2017.pdf17.pdf.

Voightländer, 2017. E-Mount 15 Mm / F 4.5 Super Wide Heliar Aspherical III. URL: (Last date Accessed: 1 Oct. 2018). https://www.voigtlaender.de/lenses/e-mount/15-mm-14-5-super-wide-heliar-aspherical-iii/?lang=en.

Whitehead, K., Hugenholtz, C., 2014. Remote sensing of the environment with small unmanned aircraft Systems (UASs), part 1: a review of progress and challenges. J. Unmanned Veh. Syst. 7, 69–85. https://doi.org/10.1139/juvs-2014-0007.

Wouda, F.J., Giuberti, M., Bellusci, G., Veltink, P.H., 2016. Estimation of full-body poses using only five inertial sensors: an eager or lazy learning approach? Sensors 16, 2138–2155. https://doi.org/10.3390/s16122138.

Zabala, S., 2017. Comparison of Multi-temporal and Multispectral Sentinel-2 and Unmanned Aerial Vehicle Imagery for Crop Type Mapping". Master of Science (MSc) Thesis in Geo-information Science and Earth Observation for Environmental Modelling and Management. June 2017. URL:. Lund University, Lund, Sweden. http://lup.lub.lu.se/luur/download?func=downloadFile&recordOId=8917610&fileOId=8917627.